Pure Appl. Geophys. 176 (2019), 2869–2886
© 2019 Springer Nature Switzerland AG
https://doi.org/10.1007/s00024-018-2082-8

Pure and Applied Geophysics

The Large Andaman Islands Earthquake of 26 June 1941: Why No Significant Tsunami?

Emile A. Okal[1]

Abstract—We present a modern seismological study of the earthquake of 26 June 1941 in the Andaman Islands, the largest pre-2004 event along that section of the India-Burma plate boundary. Despite a large conventional magnitude ($M_{PAS} = 8.1$), it generated at best a mediocre tsunami for which no definitive quantitative reports are available. We show that the 1941 earthquake took place under the Andaman accretionary prism and consisted of a composite event, whose nucleating phase had a strike-slip mechanism incompatible with a data set of spectral amplitudes of mantle Rayleigh and Love waves. Combining this initial phase with a larger normal faulting mechanism can reconcile them with *P*-wave first motions, reports of subsidence on the eastern coast of the Andaman Islands and the small amplitudes of any putative tsunami. The small tsunami results from a combination of that mechanism and of a source located under the islands themselves and in shallow water, implying a reduction in amplitude under Green's law when transitioning to a deeper basin.

Key words: Tsunami, Andaman Islands, historical earthquakes.

1. Introduction

The purpose of this article is to conduct a modern reassessment of the large 1941 earthquake in the Andaman Islands, which featured a surprisingly low tsunami (Rajendran 2013), given its conventional magnitude, $M_{PAS} = 8.1$ (Gutenberg and Richter 1954).

The Andaman Islands, located in the forearc of the northern extension of the Sumatra Trench (Cochran 2010), constitute the emerged part of a large accretionary prism approximately 400 by 100 km, with basement rocks formed in the Cretaceous and uplifted starting in the Eocene as a result of the Indian-Eurasian collision (Curray 2005).

The earthquake took place at 11:52 GMT on 26 June 1941, with an epicenter in the immediate vicinity of the Andaman Islands. In this area, the convergence between the Indian plate and the Sunda block, as determined, e.g., by the REVEL model, is extremely oblique, striking N14°E at 6.7 cm/year (Sella et al. 2002); furthermore, this motion is obviously partitioned given the abundant seismicity of the Andaman Sea, where an active spreading center is present (Fitch 1972), thus defining a "Burma" or "Andaman-Sumatra" plate sliver (Fig. 1), delineated by the northern extension of the Sumatra Fault System, which evolves into the Andaman Sea spreading center (Diehl et al. 2013).

The 1941 earthquake was originally given a "Pasadena" magnitude $M_{PAS} = 8.1$ by Gutenberg and Richter (1954). This value can be confirmed by an examination of B. Gutenberg's notepads (Goodstein et al. 1980). Richter (1958, p. 712) later proposed a significantly larger magnitude of 8.7, this discrepancy having the hallmarks of a departure from scaling laws, and suggesting that the 1941 earthquake may not be a traditional subduction event, by analogy with the case of the great 1933 Sanriku earthquake, as detailed by Okal et al. (2016, p. 1497). Abe (1981) recomputed a body-wave magnitude $m_B = 8.0$, using relatively long-period waves (8 s), and a surface-wave magnitude $M_s = 7.7$. Brune and Engen (1969) used Love wave spectral amplitudes to obtain a 100-s magnitude $M_{100} = 8.0$, corresponding to a moment $M_0 = 10^{28}$ dyn cm, according to Brune (1968, Fig. 1). Any of these values makes the 1941 event the largest earthquake along the India-Burma plate boundary since the dawn of instrumental seismology and prior to the 2004 Sumatra-Andaman mega-event. Kanamori (1977) proposed a

[1] Department of Earth and Planetary Sciences, Northwestern University, Evanston, IL 60208, USA. E-mail: emile@earth.northwestern.edu

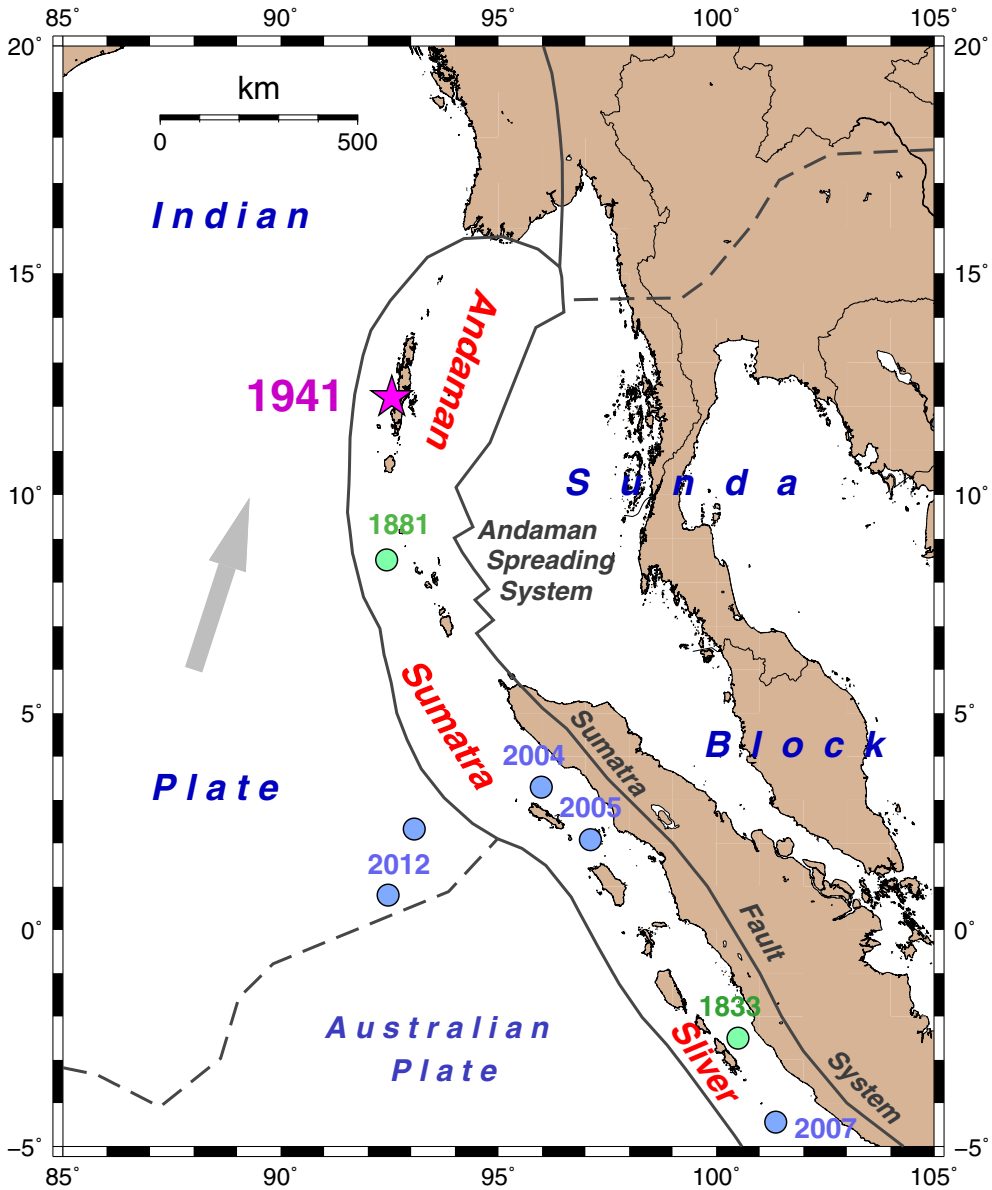

Figure 1
Sketch of the plate tectonics framework of the study area. The solid lines are plate boundaries, adapted from Bird's (2003) model. Dashed lines represent diffuse or uncertain boundaries. The large star shows the epicenter of the 1941 event and the circles those of recent (blue) and pre-instrumental (green) mega-earthquakes

significantly smaller seismic moment $M_0 = 3 \times 10^{27}$ dyn cm "from the 100-s magnitude."

A classical interpretation of the 1941 earthquake as expressing the subduction of the Indian plate under the Andaman plate (e.g., Bilham et al. 2005) gives rise to a significant problem in that the 2004 rupture propagated over its epicentral area, where it resulted in substantial seismic slip release; for example, Tsai et al.'s (2005) composite solution for the 2004 event positions a source of moment 10^{29} dyn cm only 100 km south of the 1941 event, with a slightly smaller one (8×10^{28} dyn cm) off North Andaman Island. Similarly, Ishii et al.'s (2005; Fig. 4) reverse imaging source tomography features a density of seismic

release (per unit area) over the Andaman Islands of 65–70% of its maximum along the whole rupture. These results were confirmed, e.g., by the inversion of GPS data, which suggested slips on the order of 7–10 m (e.g., Chlieh et al. 2007) and by a combined inversion of GPS, tide gauge and satellite altimetry data, requiring slips of 7–12 m in the same area (Lorito et al. 2010). All these estimates of displacement in 2004 are at least twice the slip accumulated during the 63 years separating the 1941 and 2004 events, even under the assumption of a non-partitioned boundary taking up the full convergence between the Indian and Sunda plates; they suggest that the 1941 event was not an interplate thrust earthquake.

The tsunami generated by the 1941 Andaman earthquake constitutes another, highly controversial issue. Murty (1984) reported the observation of a tsunami with an amplitude of 0.75–1.25 m on the eastern coast of India (from unspecified sources), and later Murty and Rafiq (1991) suggested that it resulted in 5000 deaths in India. However, Ortíz and Bilham (2003) and Bilham et al. (2005) have failed to unravel any scientific or press evidence to support this assertion (in contrast, e.g., to the Car Nicobar event of 1881), casting strong doubt on its veracity: it is extremely unlikely that a 1–m tsunami would result in such a death toll. It would make it the most lethal tsunami in the far field in the twentieth century and the second or third most lethal one regardless of distance, surpassed clearly only by the 1952 Kamchatka event, a seismologically much larger event (Smyshlyaev 2003), and perhaps comparable to the 1976 Mindanao event for which the repartition of the 5000 to 8000 casualties between earthquake and tsunami is unclear. In particular, a human disaster of this scope should have been widely reported in the press, which was not the case, as forcefully expressed by Rajendran (2013). Further, it would have required catastrophic waves at the epicenter, which have not been documented in the Andaman Islands (which in 1941 were not yet under Japanese occupation). Jhingran (1953) gives a detailed account of the macroseismic effects of the 1941 earthquake, but makes only a vague mention of a tsunami ("there is no doubt that extensive waves were forced at least around the Andaman Islands"), with no specific description at any location. Following Rajendran (2013), we conclude that the 1941 earthquake was probably not accompanied by a substantial tsunami either in the vicinity of its epicenter or a fortiori on the coast of India.

These questions motivate a fresh look at the 1941 Andaman earthquake, which is the subject of this article. We will show that the event has a composite mechanism and does not represent an episode of subduction of the Indian plate.

2. *Relocation*

The 1941 earthquake was originally located by the International Seismological Summary (ISS) at (12.4°N; 92.5°E), an epicenter simply rounded to the nearest half-degree (12.5°N; 92.5°E) by Gutenberg and Richter (1954); by contrast, the USGS solution (12.8°N; 92.7°E) is about 50 km to the north. Modern relocations include the Centennial Catalog solution (Engdahl and Villaseñor 2002) (12.149°N; 92.478°E), Bilham et al.'s (2005) (12.13°N; 92.49°E) and the ISC-GEM solution (Storchak et al. 2015) (12.017°N; 92.575°E).

We conducted our own relocation, based on the ISS data set and using the interactive iterative algorithm of Wysession et al. (1991), which yielded an epicenter at (12.21°N; 92.55°E), only 10 km from the Centennial Catalog's and 22 km from the ISC-GEM source. All these relocations are summarized in Fig. 2, which also shows our Monte Carlo confidence ellipse, obtained by injecting Gaussian noise into the data set with a standard deviation $\sigma_G = 4.5$ s, adequate for an event in the early 1940s.

We found that the ISS data set of arrival times cannot constrain depth, a conclusion shared by Storchak et al. (2015), who used a fixed depth (20 km); by contrast, Engdahl and Villaseñor (2002) proposed a floated depth of 49 km. In Fig. 3a, and following Rees and Okal (1987), we examine the r.m.s. residuals for constrained-depth relocations, as a function of source depth; we find a very weak increase with depth, suggestive of a shallow source, but with no resolvable trend in the first ~ 40 km. The minimal moveout of the resulting epicenters is shown by the small open circles in Fig. 2 and in cross section in

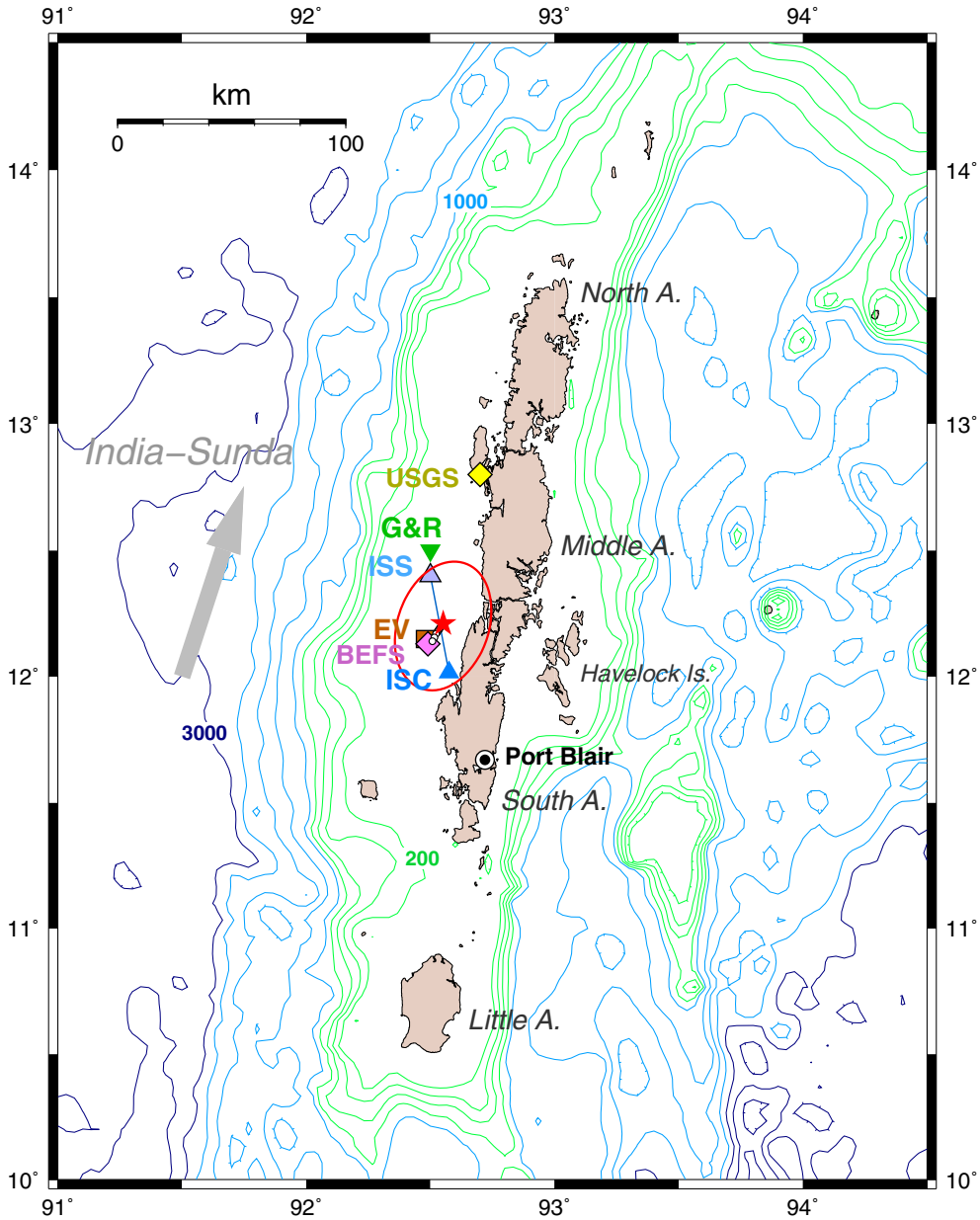

Figure 2

Relocation of the 1941 mainshock. Our relocation is shown as the red star, together with its Monte Carlo ellipse. The small open circles show the minimal moveout of the epicenter as a function of constrained source depth, from 20 to 150 km. ISS (light blue) and relocated ISC-GEM (dark blue) solutions shown as triangles, Gutenberg and Richter's (1954) as an inverted green triangle, Engdahl and Villaseñor's (2002) as a brown square and Bilham et al.'s (2005) as a magenta diamond; the USGS location is the yellow diamond. Isobaths every 200 m (green), then from 1000 m every 500 m (blue). The large gray arrow on the left shows the motion of India with respect to Sunda in the REVEL model (Sella et al. 2002)

Fig. 3b against a background of unrelocated seismicity (1963–2015; 11°N–14°N; $M > 5$), defining a seismogenic zone extending to $\sim$40 km; in this context, the 49-km depth proposed by Engdahl and Villaseñor (2002) may be acceptable, but could also be an artifact of interpreting secondary arrivals as

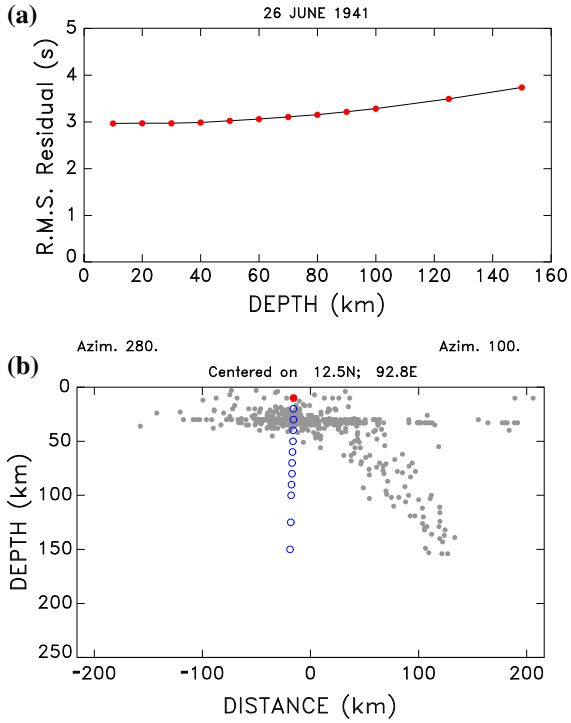

Figure 3
a Variation of r.m.s residual as a function of depth for constrained-depth relocations of the 1941 mainshock. Note lack of resolution above 40 km. **b** Cross section of epicentral area along the azimuth 280°–100°. The red dot is the preferred relocation, the open blue circles the hypocentral solutions obtained at constrained depths from 20 to 150 km. Background seismicity from NEIC catalog (1970–2016) in gray, suggesting a depth less than 40 km

depth phases because of the source complexity which will be documented below. At any rate, the lack of resolution of hypocentral depth prevents a definitive positioning of the source with respect to the plate interface.

It is remarkable that all proposed epicenters (and our confidence ellipse) are located on the accretionary shelf, as defined in Fig. 2 by the 200-m contour, and mostly on its submerged part, below sea level.

2.1. Aftershocks

Table 1 and Fig. 4 detail our relocation solutions for the mainshock and 16 aftershocks occurring within the remainder of 1941 from travel-time data listed by the ISS. We label them as "post-shocks" (Code P), as opposed to genuine aftershocks (Code A), events relocating outside the cluster of confidence ellipses and interpreted as triggered by stress transfer outside the zone of rupture of the mainshock; note in particular that Event P3 is the only one (with P15, about 200 km away) relocating outside the Andaman ridge. Only two genuine aftershocks (A11 and A13) were assigned magnitudes (in both instances, $M_{\mathrm{PAS}} = 6.0$); they are shown in blue. They can be assumed to be the largest aftershocks; significantly, they seem to occur at the southern boundary of the fault area, thus supporting, in the case of this large event, the model of Ebel and Chambers (2016) obtained for smaller intraplate earthquakes.

Figure 4 suggests a fault area extending approximately 150 km × 80 km, which would correspond to a moment on the order of 1.6×10^{28} dyn cm assuming that the earthquake follows scaling laws (Geller 1976).

3. Focal Mechanism

A focal mechanism of the 1941 earthquake (hereafter "RV") was compiled by Ritsema and Veldkamp (1960) using polarities of P and S waves, based on questionnaires sent to worldwide stations; a modern description of its geometry features a very shallow angle thrust: ($\phi = 56°$, $\delta = 5°$, $\lambda = 90°$). However, the authors comment that the mechanism is poorly constrained, with "great possible variation" in the null axis and one of the planes. Wickens and Hodgson (1967, p. 43) later optimized this solution and proposed comparable mechanisms ("WH1", $\phi = 81°$, $\delta = 1°$, $\lambda = 117°$; "WH2", $\phi = 64°$, $\delta = 17°$, $\lambda = 100°$). For the purpose of tsunami simulations, Ramana Murthy et al. (2011) and Srivastava et al. (2012) proposed low-angle thrust mechanisms ("RM", $\phi = 20°$, $\delta = 20°$, $\lambda = 90°$; "SR", $\phi = 356°$, $\delta = 12°$, $\lambda = 90°$, respectively), but did not detail their sources.

We were able to read a data set of 15 P-wave first motions on copies of records at teleseismic stations, complemented by three polarities reported to the ISS for which records could not be inspected, with all pertinent information listed in Table 2. As shown in Fig. 5, this data set constrains the solution from this study ("TS") to a strike-slip mechanism ($\phi = 290°$,

Table 1

Events relocated in this study

Code of event	Date D M (J) Y	Origin Time (GMT)	Latitude (°N)	Longitude (°E)	Arrival times		r.m.s (s)	Magnitude M_{PAS}
					Read	Kept		
M1	**26 JUN (177) 1941**	**11:52:00.5**	**12.21**	**92.55**	**96**	**95**	**2.97**	**8.1**
A2	27 JUN (178) 1941	07:32:46.2	12.11	92.56	17	14	4.58	
P3	27 JUN (178) 1941	08:32:19.2	11.87	91.93	24	22	4.86	
A4	27 JUN (178) 1941	19:04:04.8	11.73	92.73	15	11	4.47	
A5	28 JUN (179) 1941	17:55:22.3	12.21	93.40	15	14	3.47	
A6	28 JUN (179) 1941	23:07:17.2	9.62	90.00	10	9	4.00	
A7	30 JUN (181) 1941	03:13:42.9	12.78	92.72	9	9	5.47	
A8	30 JUN (181) 1941	18:23:32.6	12.04	92.69	34	34	3.92	
A9	02 JUL (183) 1941	02:42:03.4	11.99	93.03	18	18	3.57	
A10	09 JUL (190) 1941	00:39:10.0	12.23	93.16	13	13	4.15	
A11	14 JUL (195) 1941	02:02:26.7	11.88	92.79	24	23	4.26	6.0
A12	21 JUL (202) 1941	20:19:30.0	12.47	92.63	13	11	2.73	
A13	09 AUG (221) 1941	22:17:37.7	12.06	92.79	37	35	5.21	6.0
A14	19 AUG (231) 1941	16:19:28.9	8.41	93.36	34	33	5.51	
P15	30 AUG (242) 1941	16:44:33.7	10.73	94.35	26	21	2.82	
A16	21 SEP (264) 1941	18:53:32.0	12.68	92.77	14	12	3.90	
A17	23 OCT (296) 1941	21:02:35.9	12.61	93.27	15	12	3.46	

$\delta = 80°$, $\lambda = 171°$), rotated 89° from Ritsema and Veldkamp's (1960) in the formalism of Kagan (1991) and similarly 92°, 87°, 99° and 105° from mechanisms WH1, WH2, RM and SR, respectively (out of a maximum of 120°). This very significant difference from previously published mechanisms must be considered robust, given the adequate distribution of stations on the focal sphere (see Fig. 5), whose overwhelming majority were read individually as part of this study.

In anticipation of the results of Sect. 4, we emphasize that the TS mechanism is derived from first-motion *P* waves and as such characterizes only the nucleation of the event, which will prove to be a complex earthquake; in particular, it will be found to be incompatible with long-period surface wave spectral amplitudes.

4. *Estimation of Long-Period Seismic Moment and Low-Frequency Mechanism*

Table 3 lists mantle waves for which we obtained scans of records, which we digitized and processed through the M_m mantle magnitude algorithm (Okal and Talandier 1989). Results are shown in Fig. 6 in terms of the magnitude M_c corrected for the focal mechanism TS, obtained from the first motions in Sect. 3. That focal geometry clearly misfits the distribution of spectral amplitude among stations, with, for example, Rayleigh and Love waves at COL requiring moments differing by $\sim$2.5 orders of magnitude, as do Love waves at HON and TUC.

We are thus drawn to envision that the 1941 event must have featured a composite focal mechanism, with the first arrivals controlled by an initial strike-slip mechanism, followed by a main event with a different geometry controlling the spectral amplitude of mantle waves. We attempted to invert the mantle magnitude data set using the PDFM method (Reymond and Okal 2000), which we have successfully applied to a number of historical events (e.g., Okal 2005), but, unfortunately, we could not obtain a stable inversion. In this context, we resorted to a trial-and-error method to constrain the low-frequency mechanism of the 1941 earthquake.

In the introduction, we pointed out that significant moment release over the Andaman Islands during the 2004 event suggests that the 1941 earthquake was not a typical low-angle thrust event at the subduction interface and thus the main non-strike-slip component of its mechanism cannot be inferred simply by the plate tectonic context. We verified in particular that the focal geometry of the great 2004 earthquake does

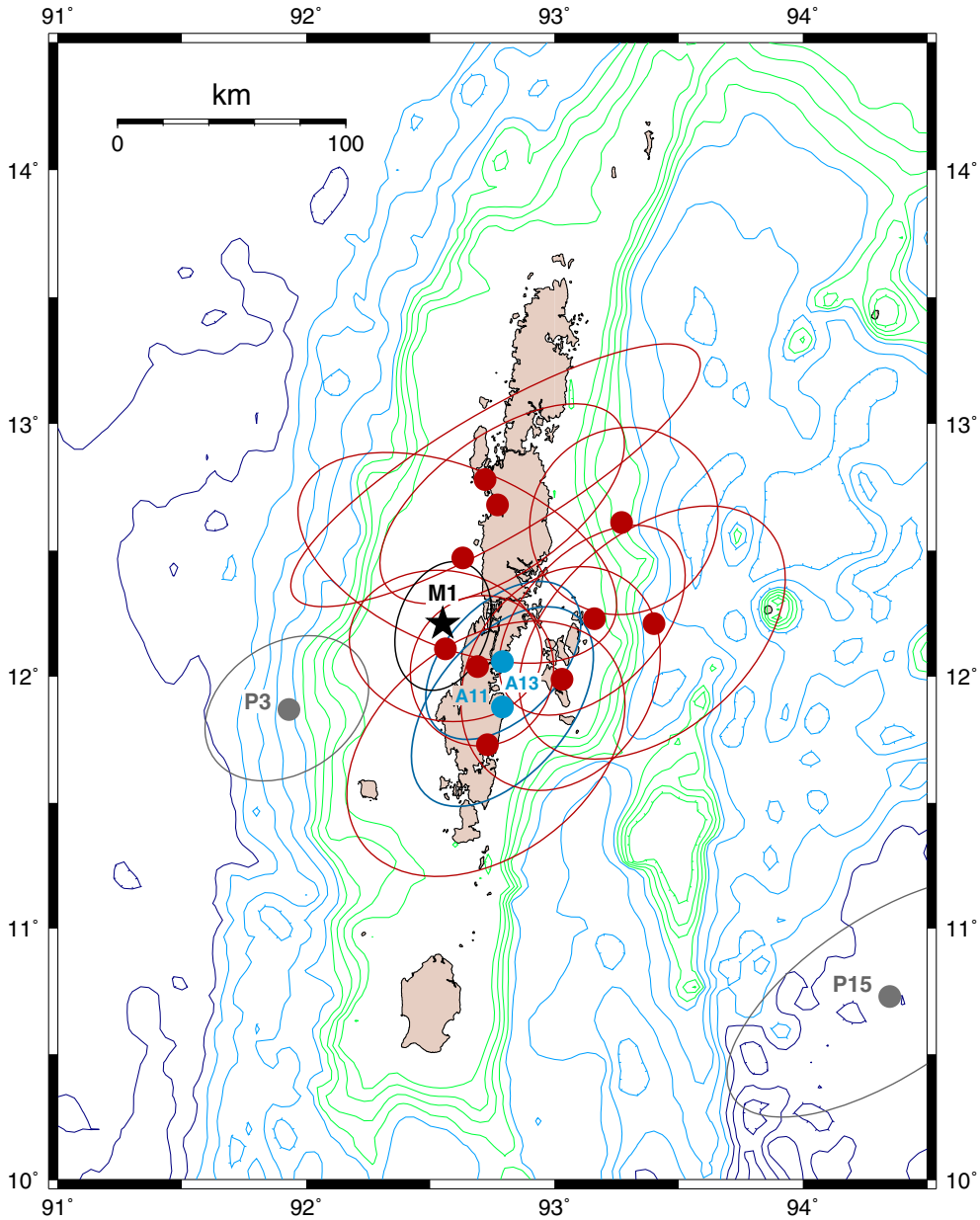

Figure 4
Map of relocations for the 17 events listed in Table 1. Each event is shown as its preferred epicenter, surrounded by its Monte Carlo ellipse. Genuine aftershocks are shown in dark red, the two large ones with a published magnitude in blue and the "postshocks" triggered by stress outside of the presumed rupture zone in gray; the mainshock is shown as the black star. See text for details

not fit our spectral amplitudes, with the Love waves at CTO and COL requiring moments varying by 2.5 orders of magnitude.

Faced with this condition, we explored the distribution of focal mechanisms in the background seismicity of the epicentral area. For this purpose, we extracted from the Global CMT catalog (Dziewonski et al. 1981; Ekström et al. 2012) all 64 shallow solutions ($h \leq 100$ km) in a box delimited by latitudes 11°N–14°N and longitudes 92°E–93.5°E; we

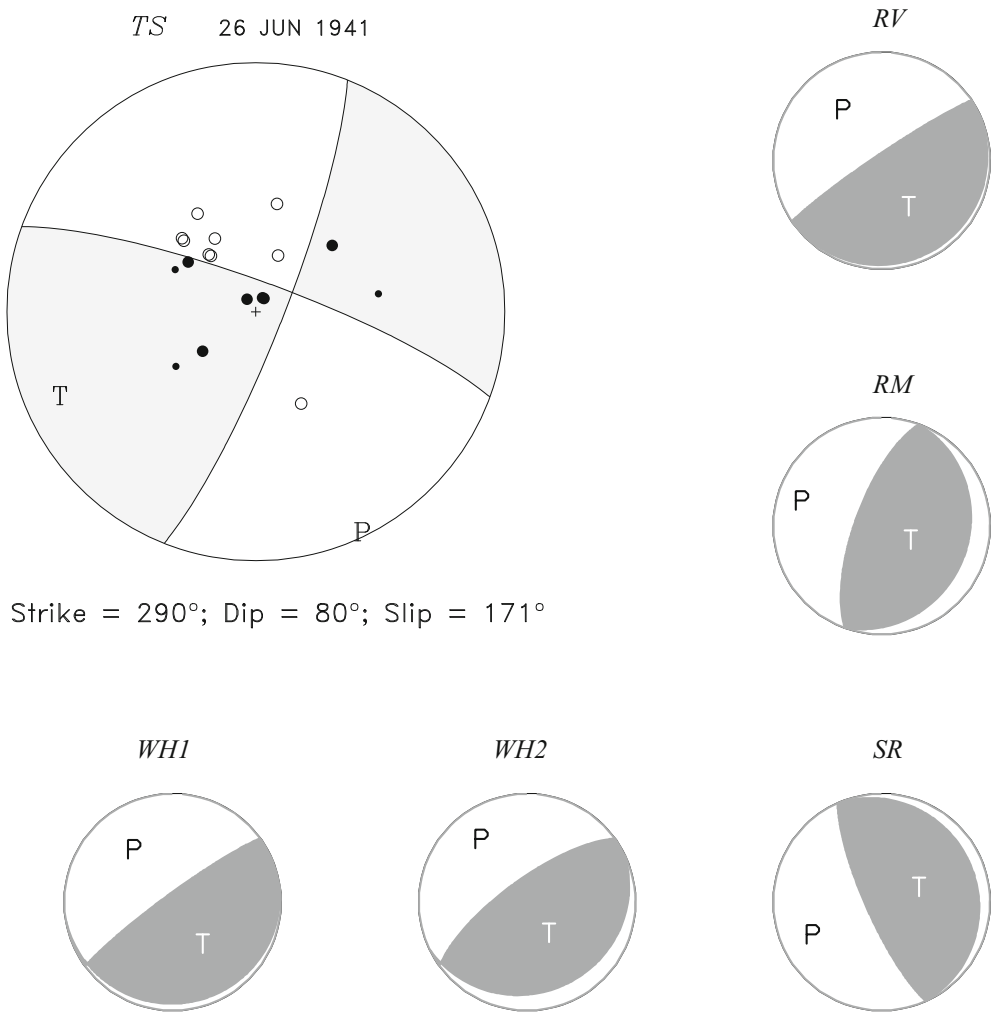

Figure 5
Top left (TS): focal mechanism obtained in this study from *P*-wave first motions. Solid dots represent upwards (anaseismic) first motions, open dots downwards (kataseismic) ones; smaller symbols relate to data retrieved unverified from the ISS. Bottom and right: mechanisms proposed in previous studies. See text for details

regard them as representative of stresses existing in the vicinity of the 1941 epicenter. We note that an overwhelming majority of these events (46 out of 64) took place in the aftermath of the great 2004 earthquake, presumably as the result of stress transfer. We further classify them as strike-slip (15 events), normal (13) or thrust (18) if their null, compressional or tensional axes, respectively, dip more than 50°; the remaining 18 events are considered hybrid. This classification is inspired by the formalism of ternary diagrams introduced by Frohlich and Apperson (1992). In each category, we further define an average mechanism as the best double-couple of the sum of the relevant moment tensors, unweighted by scalar moment, and explore the coherence of the group by analyzing the distribution of "Kagan" angles of solid rotation (Kagan 1991) between individual events and the average mechanism; we recall that the theoretical maximum value for a Kagan angle is 120°.

Results, listed in Table 4, indicate that normal faulting events (all but one post-Sumatra) are reasonably well grouped around their average mechanism, being rotated from it an average Kagan angle of 28° ± 10°. So are thrust events, but in their

Table 2

First-motion data set used in this study

Station		Distance (°)	Azimuth (°)	First motion[b]
Code	Location[a]			
Read in this study				
TAS	Tashkent, Uzbekistan	35.5	329	d
IRK	Irkutsk, Russia	41.1	11	d
BAK	Baku, Azerbaijan	46.9	315	d
MIZ	Mizusawa, Japan	49.0	252	u
PER	Perth, Western Australia	49.4	154	d
TIF	Tbilisi, Georgia	50.9	314	d
PUL	Pulkovo, Russia	65.7	331	d
ATU	Athens, Greece	65.9	306	u
GTT	Göttingen, Germany	75.9	320	d
DBN	De Bilt, The Netherlands	78.8	321	d
CTO	Cape Town, South Africa	84.0	234	u
COL	College, Alaska	90.9	22	d
PAS	Pasadena, California	125.3 (PKP)	31	u
TUC	Tucson, Arizona	130.3 (PKP)	26	u
SJG	San Juan, Puerto Rico	143.2 (PKP)	325	u
Transcribed from ISS				
MAN	Manila, Philippines	27.8	82	u
TAN	Antananarivo, Madagascar	54.1	236	u
HLW	Helwan, Egypt	59.1	298	u

[a]Locations and countries reflect present political boundaries

[b]u: anaseismic ("up"); d: kataseismic ("down")

case, the average mechanism differs significantly (by a 57° Kagan angle) from that of the 2004 mega-earthquake, supporting the idea that these earthquakes may not be located at the subduction interface; we note also that many (11 out of 18) occurred prior to the 2004 mega-earthquake. In both instances, the average mechanism gives a fair representation of the population of geometries of strain release in the epicentral area. By contrast, the strike-slip events (all of which postdate the 2004 mega-earthquake) are more scattered in geometry, with a mean Kagan angle of 40° with respect to their average mechanism; the latter is also 70° away from the mechanism (TS) inferred from the first motions in Sect. 3. A similar conclusion is reached for the hybrid group.

In this context, we select the two average mechanisms for normal and thrust faulting events (with moment tensors $\mathbf{M_N}$ and $\mathbf{M_T}$, respectively) and recompute corrected mantle magnitudes M_c for composite mechanisms obtained by adding the moment tensor of the first motion ($\mathbf{M_{TS}}$, as derived in Sect. 3), weighted by a variable coefficient α

$$\mathbf{M}_{composite} = \alpha \mathbf{M_{TS}} + (1 - \alpha) \mathbf{M_{N,T}}. \quad (1)$$

Finally, we optimize α by trial and error, so as to minimize the scatter in the resulting M_c values. As shown in Fig. 7, the best results are obtained with the normal faulting average solution and a parameter $\alpha = 0.20$; an acceptable but less satisfactory fit is also obtained with the thrusting mechanism ($\alpha = 0.21$).

We note in Fig. 7 that neither of the two solutions features a significant increase of moment with periods, the (negative) slope of the regression of M_c with frequency being 0.04 (normal faulting) and 0.05 (thrust) logarithmic units per mHz, well within the range of typical subduction zone events; we recall (Okal and Saloor 2017; Salaree and Okal 2018) that

Table 3

Mantle waves used in the moment determination

Station		Distance (°)	Azimuth (°)	Intrument type	Phases used
Code	Location				
DBN	De Bilt, The Netherlands	78.8	321	Golitsyn	R_1, G_1, G_3
CTO	Cape Town, South Africa	84.0	234	Milne Shaw	G_1
COL	College, Alaska	90.9	22	McRomberg	R_1, G_1
AUC	Auckland, New Zealand	91.2	127	Milne-Shaw	G_1
HON	Honolulu, Hawaii	103.1	64	Milne-Shaw	R_1, G_1
PAS	Pasadena, California	125.3	31	Benioff 1–90	G_3
TUC	Tucson, Arizona	130.3	26	Benioff 1–77	G_1
SJG	San Juan, Puerto Rico	143.2	325	Wenner	G_1

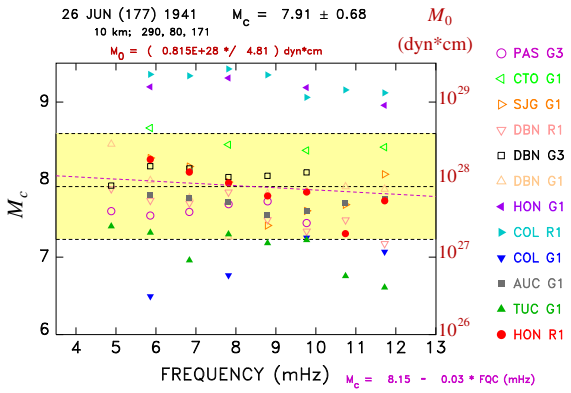

Figure 6
Mantle magnitudes M_c (Okal and Talandier 1989) corrected for the strike-slip focal mechanism obtained from first motions. The horizontal dashed line is the value averaged over all measurements and the colored band the 1–σ range. Note the widely scattered distribution of results, in particular the incompatibility between G_1 values at HON and TUC or COL

Table 4

Characteristics of background global CMT seismicity in the Andaman Islands, 1976–2018

Type	Number of events		Average mechanism			Kagan angle
	Total	Pre-2004	ϕ (°)	δ (°)	λ (°)	Average ± r.m.s. (°)
Normal	13	1	223	40	− 68	28 ± 10
Thrust	18	11	346	40	79	30 ± 10
Strike-slip	15	0	268	75	− 16	40 ± 18
Hybrid	18	5	176	84	125	46 ± 29

slow events, such as tsunami earthquakes, feature an absolute slope in excess of 0.07 logarithmic units per mHz.

In conclusion, our preferred solution is a composite focal mechanism ("NO") in which the strike-slip nucleation features the TS mechanism ($\phi = 290°$, $\delta = 80°$, $\lambda = 171°$) with a moment $M_0^{TS} = 2.2 \times 10^{27}$ dyn cm followed by a normal faulting event ($\phi = 214°$, $\delta = 54°$, $\lambda = -68°$) with a moment $M_0^{NF} = 8.7 \times 10^{27}$ dyn cm. An alternative solution ("TH") could feature a moment $M_0^{TS} = 2.5 \times 10^{27}$ dyn cm for the *TS* nucleation, followed by a thrust faulting event ($\phi = 346°$, $\delta = 40°$, $\lambda = 79°$) with a moment $M_0^{TF} = 9.6 \times 10^{27}$ dyn cm. Either of these combinations

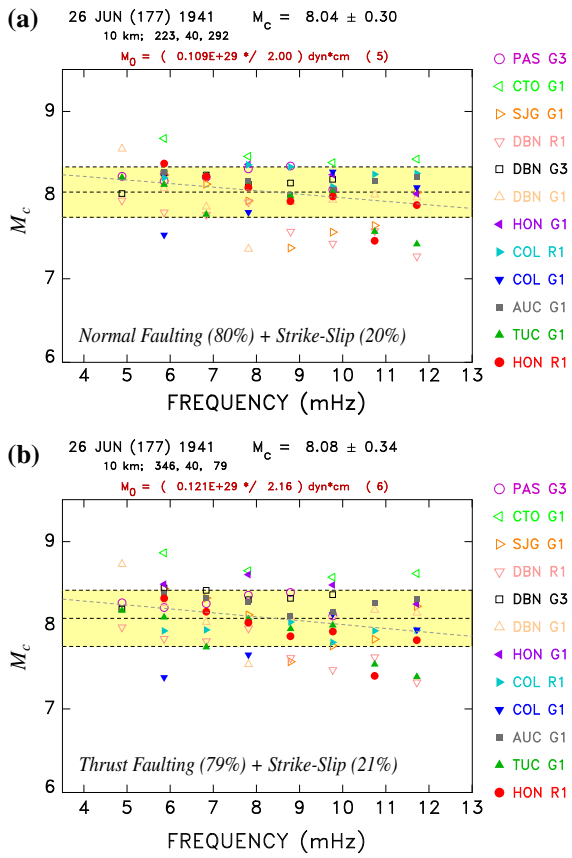

Figure 7
a Same as Fig. 6 for the preferred mechanism obtained by combining the average normal faulting mechanism ($\phi = 223°$; $\delta = 40°$; $\lambda = -68°$; weighted 80%) with the first-motion strike-slip mechanism, weighted 20%. Note the much reduced scatter. **b** Same as **a** for the average thrust faulting mechanism. See text for details

reconciles the data set of the first motions obtained in Sect. 3 with the spectral amplitudes of mantle waves at the eight stations listed in Table 3. Figure 8 illustrates the combination of mechanisms involved in the NO and TH mechanisms. We emphasize, however, that the final "beachballs" for the composite mechanisms do not represent the distribution of first motions on the focal sphere, since the main non-strike-slip component of the source is expected to be delayed.

While the data set of spectral amplitudes of mantle waves cannot discriminate between the mainly normal ("NO") and thrust ("TH") mechanisms, we turn our attention to the static offsets described by Jhingran (1953), who reported

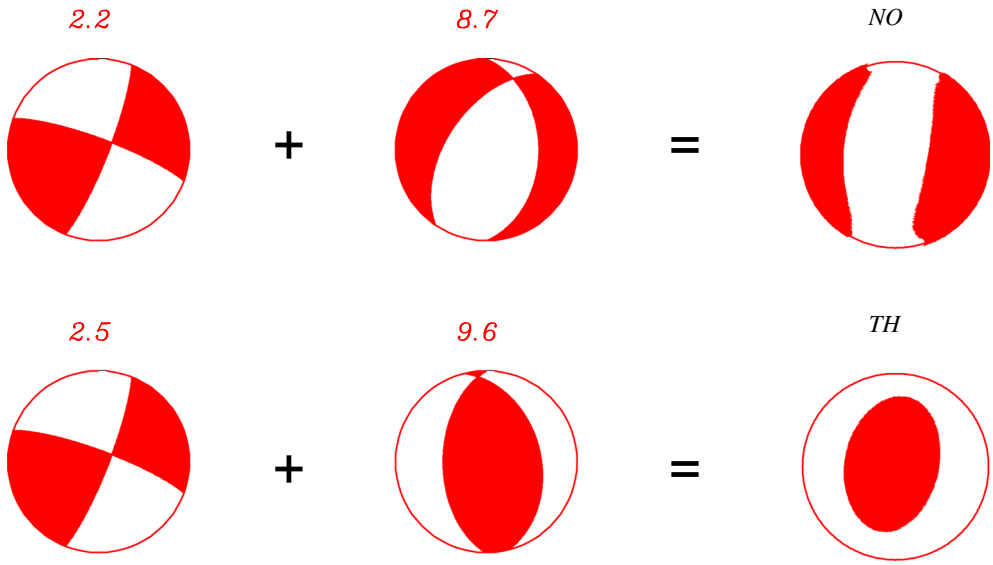

Figure 8
Top: illustration of the combination of the nucleating strike-slip mechanism (left) and of the average background normal faulting double-couple (center) resulting in the preferred "NO" composite mechanism (right). Bottom: same for the "TH" mechanism. The small numbers above the beachballs represent the seismic moments (in units of 10^{27} dyn cm) used in the various combinations. See text for details

subsidence of ~ 70 cm ("$2-2\frac{1}{2}$ ft.") at Port Blair and farther north along the eastern coast of the main island group at a number of locations that we have identified as lying between latitudes 12.10°N and 12.40°N. By contrast, and despite a report of more extensive damage, Jhingran (1953) mentions no vertical motion on the much less populated west coast.

In Fig. 9, we compute static displacements due to the "TH" and "NO" mechanisms using the formalism of Mansinha and Smylie (1971). The computations are performed by superimposing the fields produced by the two components to the source, as described by Eq. (1). An additional complexity stems from a possible lateral offset between the strike-slip precursor and the mainshock; in this context, Fig. 9 represents the results of a trial-and-error search optimizing fits to both the above reports of static motion and the tsunami simulations in Sect. 5 for which they serve as initial conditions.

A robust property of the mechanisms tested is that, regardless of the lateral offset between the two components, a "TH" mechanism produces a strong uplift flanked by areas of marginal subsidence (Fig. 9b), while an "NO" mechanism results in a strong subsidence flanked by minor uplift. In this context, the reports of systematic subsidence extending from Port Blair to the north clearly favor the "NO" geometry and cannot be reconciled with a "TH" mechanism. The preferred mechanism shown in Fig. 9a features a normal component offset 40 km in the azimuth N135°E from the nucleation epicenter. It does replicate the subsidence reports and concentrates most of the vertical deformation on the Andaman ridge (loosely defined as the 200-m isobath, in red in Fig. 9, which will play an important role in the inefficient generation of the tsunami (see Sect. 5 below).

5. *Tsunami Simulations*

In this section, we use the composite mechanisms derived in Sect. 4 to simulate the generation of a tsunami in the Bay of Bengal and the Andaman Sea, and its propagation in the Indian Ocean, seeking in particular to explain the absence of confirmed reports of significant inundation during the 1941 earthquake.

Our simulations use the MOST algorithm (Titov and Synolakis 1998; Titov et al. 2016), which solves

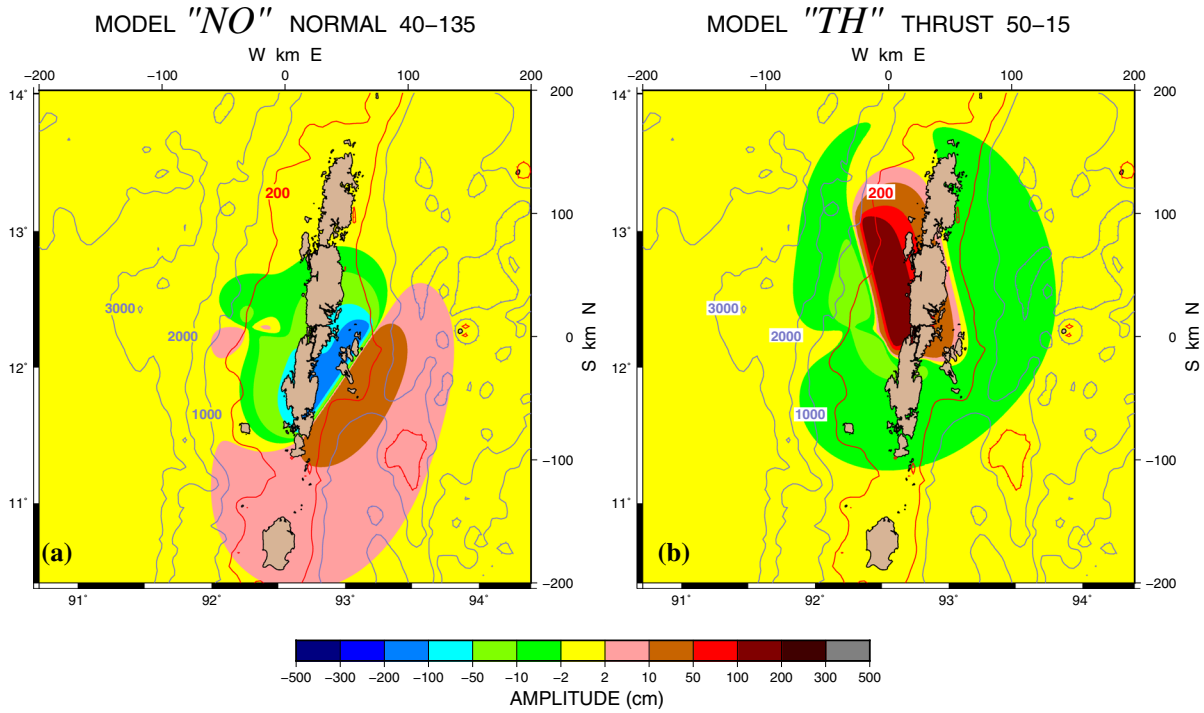

Figure 9
a Field of static displacements $\eta(x, y; 0_+)$ for the composite mechanism "NO", featuring a normal faulting mainshock offset 40 km in the azimuth N135°E from the strike-slip nucleator, superimposed on morphologic and bathymetric data. The red contour outlines the 200-m isobath, the dark blue ones the 1000-m, 2000-m and 3000-m ones. Note that most of the deformation occurs within the range of the 200-m isobath. **b** Same as **a** for the thrust model "TH". See text for details

the full non-linear equations of hydrodynamics under the shallow-water approximation, by finite differences and through the method of alternate steps (Godunov 1959). MOST has been extensively validated through comparisons with laboratory and field data, per standard international protocols (Synolakis et al. 2008); full details can be found in Synolakis (2003).

As initial conditions for the vertical displacements of the sea surface, $\eta(t = 0_+)$, we use the field of static deformations resulting from the seismic dislocation, computed through the algorithm of Mansinha and Smylie (1971) in the geometry of a homogeneous half-space. This approximation is appropriate as the rise time of an earthquake is always much shorter than the characteristic time needed by a tsunami wave to flush the displaced water out of the generation area (e.g., Saito and Furumura 2009; Dalrymple and Derakhti 2018). For the composite mechanisms used in the present study, we superimpose the fields of deformation of the two individual subevents. In the absence of information on any possible spatial offset between the two subevents, we start by simply locating both at our preferred epicenter (12.21°N; 92.55°E). The simulation uses a 5-arcmin grid and a 10-s time step, satisfying the CFL stability condition (Courant et al. 1928); it is carried on for 5000 s and is stopped at the 20-m isobath in the vicinity of coastlines.

Figure 10 shows the results of our simulation for the normal faulting composite mechanism in the form of the field of maximum amplitudes $\eta_{\max}$ of vertical water displacement during the simulated 5000-s window. The tsunami remains very small ($\eta_{\max} < 3$ cm) over most of the Bay of Bengal and does not leak into the main Indian Ocean Basin. It remains smaller than 10 cm at the 20-m isobath where the computation is stopped, off most of the coastlines across the Bay of Bengal. In the Andaman Islands, it predictably affects mostly the western

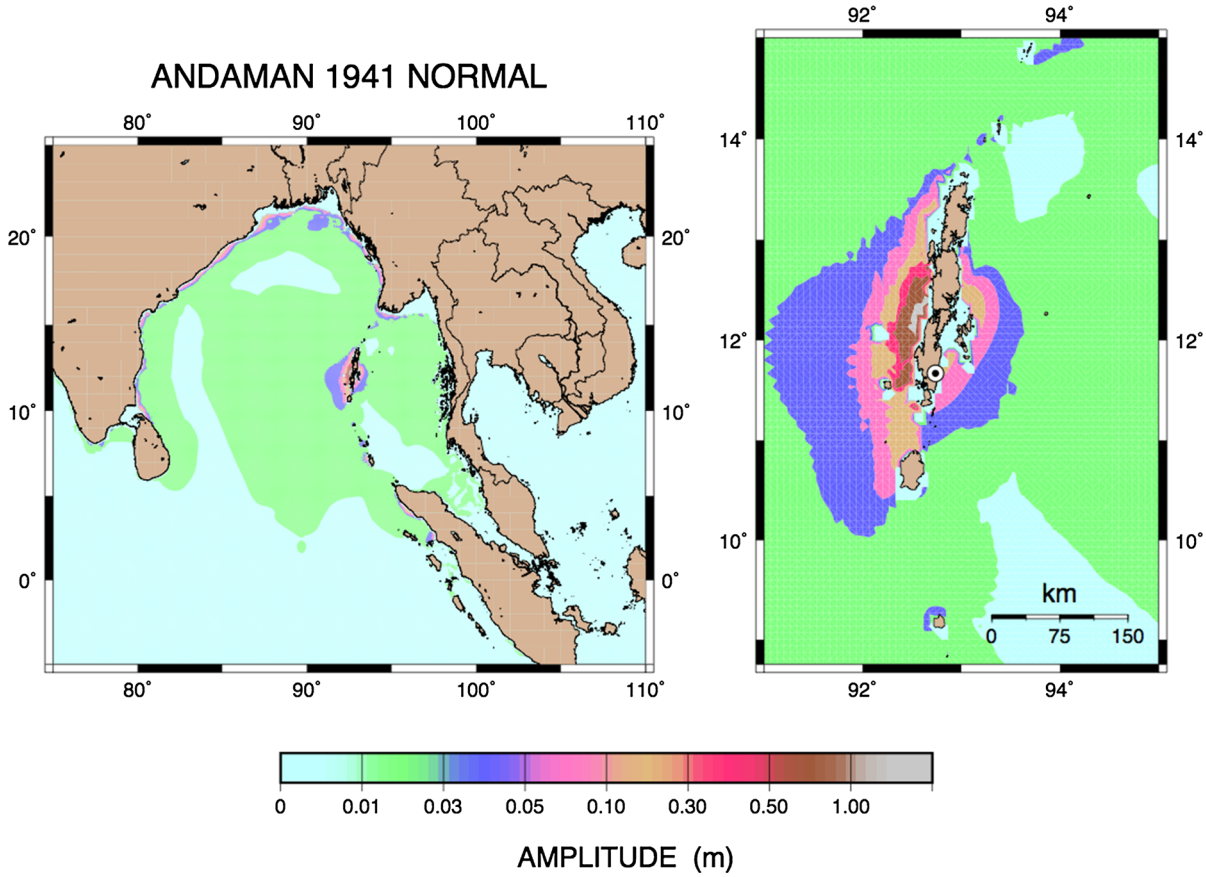

Figure 10
Maps of the field of maximum amplitudes η_{max} for the composite normal faulting mechanism. Left: Bay of Bengal and adjoining areas. Right: close-up around the Andaman Islands. The computation is stopped at the 20-m isobath. The bull's eye symbol shows the location of the capital and main population center, Port Blair

coasts, which in 1941 were far less populated that the eastern ones, and remain to this day. The tsunami amplitude on the high seas off the main city of Port Blair remains centimetric.

Similarly, Fig. 11 presents the field η_{max} for the thrust composite mechanism. Amplitudes along the shorelines of the Bay of Bengal reach observable levels ($\sim$15 cm at the 20-m isobath) along some eastern shores of India. In the Andaman Islands, the maxima are generally smaller on the eastern coasts and larger on the western ones.

In Fig. 12, we consider the preferred composite source "NO" described in Sect. 4, which features a spatial offset of 40 km in the N135°E azimuth between the nucleating strike-slip mechanism and the main normal faulting component. Under this scenario, the amplitudes at the 20-m isobath along the Indian and Western Burmese coasts are reduced to about 2 cm, while they are slightly increased, to about 5 cm, along the eastern shores of the Andaman Sea, in Eastern Burma and Western Thailand. In the Andaman Islands, the distribution of η_{max} is also altered, with larger amplitudes on the eastern shores and reduced ones in the west. On the eastern shores, where the population (and hence the potential for observation) was highest, e.g., in Port Blair, the 20-m amplitudes reach about 30 cm. In Fig. 13, we move the thrust fault component of the "TH" mechanism 50 km in the N15°E direction. Again, the general pattern of η_{max} is retained, with this time smaller amplitudes on the shores of the Bay of Bengal and

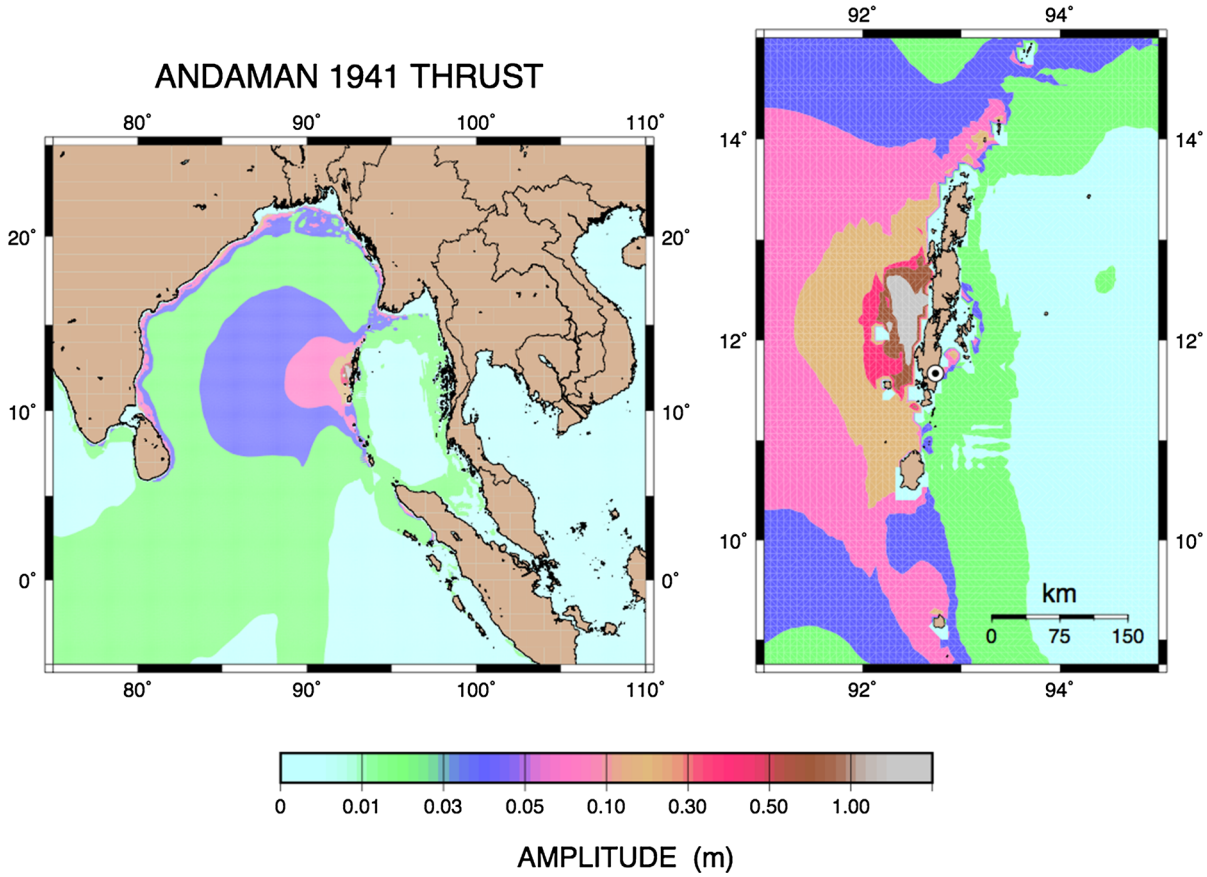

Figure 11
Same as Fig. 10 for the composite thrust mechanism

especially on the eastern coasts of the Andaman Islands.

In very general terms, all our simulations predict rather deceptive amplitudes for an earthquake with a total moment of 10^{28} dyn cm. In physical terms, we can identify several reasons contributing to a reduction of η_{max}, in both the near field (on the islands) and far field, across the Bay of Bengal. The mere presence of the Andaman Islands significantly reduces the area of ocean floor where water is displaced coseismically; in simple terms, the earthquake moves more rock and less water. This situation is strikingly reminiscent of the geometry of the 2005 Nias earthquake, whose domain of rupture was significantly overlain by emerged land, namely the Nias and Simeulue Islands. Because of its much larger size, the 2005 earthquake did generate a significant tsunami; however, it did not reach the catastrophic proportions that its moment [1.4×10^{29} dyn cm (Okal and Stein 2009)] would have suggested, especially in the near field where considerable damage was wrought by the earthquake (Boen 2006).

In addition, the remainder of the source area of the 1941 earthquake is located under very shallow water, most of it < 200 m deep (Fig. 9). As a result, the tsunami falters according to Green's (1837) law, when it transitions to the deeper waters of the Bay of Bengal. This situation is again reminiscent of the 2005 Nias event, which produced a negligible tsunami in the far field, despite its large seismic moment (Okal and Synolakis 2008). Finally, the composite nature of the focal mechanism, involving a strike-slip component of about 1/5 of the total moment, reduces the vertical deformation in the epicentral area, and hence the amplitude of the tsunami, especially in the near field.

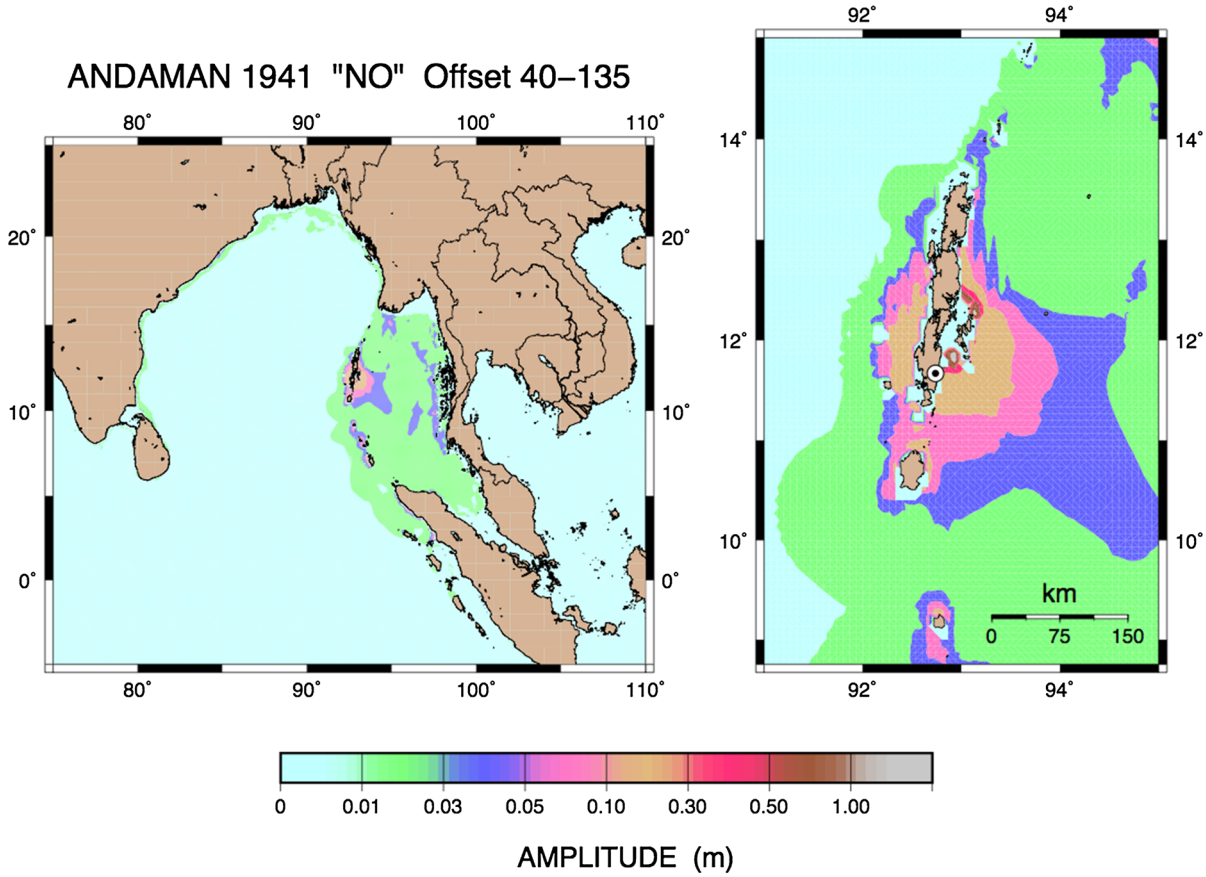

Figure 12
Same as Fig. 10 for a composite normal mechanism, where the normal component is moved 40 km in the N135°E direction

From the observational standpoint, and for all the models envisioned, the tsunami amplitudes at the 20-m depth where the computations are terminated are larger on the western shores of the Andaman Islands, away from the populated centers including the main city of Port Blair, which are located on the eastern shores.

6. *Conclusion*

We have revisited the 1941 Andaman earthquake, the largest in the 20th century in that part of the India-Burma plate boundary. We conclude that it cannot be interpreted as an interplate thrust event expressing the subduction of the Indian plate. The distribution of its teleseismic first motions requires nucleation as a strike-slip mechanism, which is however incompatible with the spectral amplitudes of Rayleigh and Love waves at mantle periods, thus requiring a composite mechanism. We prefer a normal faulting geometry for the main part of the source, as it can fit the coseismic subsidence reported on the eastern coast of the islands. That model predicts small tsunami amplitudes along the coasts of the Bay of Bengal, supporting the results of Ortíz and Bilham (2003), who failed to document any scientific or press reports of a substantial tsunami in India; it is also generally compatible with Jhingran's (1953) qualitative statement about "extensive waves…around the Andaman Islands."

We emphasize again that our models are by no means unique, and we do not pretend that our preferred one ("NO"; Figs. 9a, 12) is necessarily representative of the true mechanism of the event. Our purpose is merely to show that it is possible to

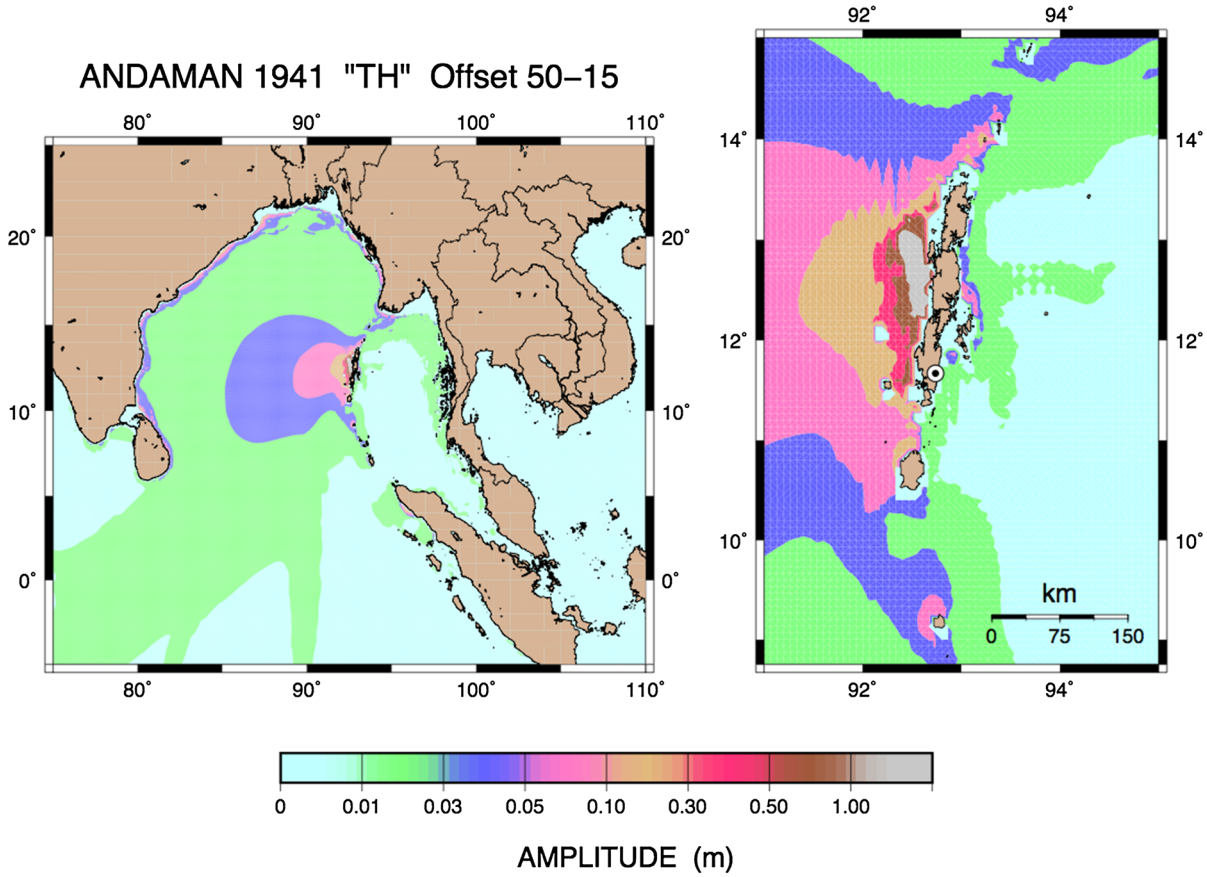

Figure 13
Same as Fig. 11 for a composite thrust mechanism, where the thrust component is moved 50 km in the N15°E direction

build one (or several) models that can reconcile the seismological data (first motions of body waves and spectral amplitudes of surface waves at mantle periods), Jhingran's (1953) reports of subsidence on the eastern shore of the Andaman Islands and the mediocre amplitudes of any putative tsunami.

We stress that the existence of major earthquakes deviating from an interplate thrust geometry is a common occurrence at subduction zones, especially those featuring oblique subduction. A further example would be the West Aleutian subduction zone, where mechanisms of all kinds (thrust, normal, strike-slip, hybrid) are well documented in modern-day seismicity.

Finally, this study reaffirms, if need be, the value of historical records in sharpening our understanding of tectonic processes at major plate boundaries, where the recurrence times of significant earthquakes can be much longer than the present extent of modern digital networks, even when combined with their analog predecessor, the World-Wide Standardized Seismic Network (Okal 2015).

Acknowledgements

We are grateful to Ian Saunders (Pretoria), Bernard Dost (De Bilt) and Brian Ferris (Lower Hutt) for access to the excellent seismological archives at their respective facilities. Some figures were drawn using the GMT software (Wessel and Smith 1991). The paper benefited from the constructive comments of two anonymous reviewers.

Publisher's Note Springer Nature remains neutral with regard to jurisdictional claims in published maps and institutional affiliations.

References

Abe, K. (1981). Magnitudes of large shallow earthquakes from 1904 to 1980. *Physics of the Earth and Planetary Interiors*, *27*, 72–92.

Bilham, R., Engdahl, E. R., Feldl, N., & Satyabala, S. P. (2005). Partial and complete rupture of the Indo-Andaman plate boundary, 1847–2004. *Seismological Research Letters*, *76*, 299–311.

Bird, P. (2003). An updated digital model of plate boundaries. *Geochemistry, Geophysics, Geosystems*, *4*(3), GC000252.

Boen, T. (2006). Sructural damage in the March 2005 Nias-Simeulue earthquake. *Earthquake Spectra*, *22*, S419–S434.

Brune, J. N. (1968). Seismic moment, seismicity, and rate of slip along major fault zones. *Journal of Geophysical Research*, *73*, 777–784.

Brune, J. N., & Engen, G. R. (1969). Excitation of mantle Love waves and definition of mantle wave magnitude. *Bulletin of the Seismological Society of America*, *59*, 923–933.

Chlieh, M., Avouac, J.-P., Hjörleifsdóttir, V., Song, T.-R. A., Ji, C., Sieh, K., et al. (2007). Coseismic slip and afterslip of the great $M_w = 9.15$ Sumatra-Andaman earthquake of 2004. *Bulletin of the Seismological Society of America*, *97*, S152–S173.

Cochran, J. R. (2010). Morphology and tectonics of the Andaman Forearc, Northeastern Indian Ocean. *Geophysical Journal International*, *182*, 631–651.

Courant, R., Friedrichs, K., & Lewy, H. (1928). Über die partiellen Differenzengleichungen der mathematischen Physik. *Mathematische Annalen*, *100*, 32–74.

Curray, J. R. (2005). Tectonics and history of the Andaman Sea region. *Journal of Asian Earth Sciences*, *25*, 187–232.

Dalrymple, R.A., & Derakhti, M. (2018). Tsunami generation by earthquakes: Seabed topography and inertial effects. In: *Proceedings 36th international conference on coastal engineering*, 1605, Baltimore [abstract].

Diehl, T., Waldhauser, F., Cochran, J. R., Kamesh Raju, K. A., Seeber, L., Schaff, D., et al. (2013). Back-arc extension in the Andaman Sea: Tectonic and magmatic processes imaged by high-precision teleseismic double-difference earthquake relocation. *Journal of Geophysical Research: Solid Earth*, *118*, 2206–2224.

Dziewonski, A. M., Chou, T. A., & Woodhouse, J. H. (1981). Determination of earthquake source parameters from waveform data for studies of global and regional seismicity. *Journal of Geophysical Research*, *86*, 2825–2852.

Ebel, J. E., & Chambers, D. W. (2016). Using the locations of $M \geq 4$ earthquakes to delineate the extents of the ruptures of past major earthquakes. *Geophysical Journal International*, *207*, 862–875.

Ekström, G., Nettles, M., & Dziewoński, A. M. (2012). The global CMT project, 2004–2010: Centroid moment tensors for 13,107 earthquakes. *Physics of the Earth and Planetary Interiors*, *200*, 1–9.

Engdahl, E. R., & Villaseñor, A. (2002). Global seismicity: 1900–1999. In *International earthquake and engineering seismology Part A* (pp. 665–690). New York: Elsevier.

Fitch, T. J. (1972). Plate convergence, transcurrent faults, and internal deformation adjacent to Southeast Asia and Western Pacific. *Journal of Geophysical Research*, *77*, 4442–4460.

Frohlich, C., & Apperson, K. D. (1992). Earthquake focal mechanisms, moment tensors, and the consistency of seismic activity near plate boundaries. *Tectonics*, *11*, 279–296.

Geller, R. J. (1976). Scaling relations for earthquake source parameters and magnitudes. *Bulletin of the Seismological Society of America*, *66*, 1501–1523.

Godunov, S. K. (1959). Finite difference methods for numerical computations of discontinuous solutions of the equations of fluid dynamics. *Matematicheskiĭ Sbornik*, *47*, 271–295.

Goodstein, J. R., Kanamori, H., & Lee, W. H. K. (1980). Seismology microfiche publications from the Caltech archives. *Bulletin of the Seismological Society of America*, *70*, 657–658.

Green, G. (1837). On the motion of waves in a canal of variable depth. *Cambridge Philosophical Transactions*, *6*, 457–462.

Gutenberg, B., & Richter, C. F. (1954). *Seismicity of the Earth and associated phenomena*. Princeton: Princeton University Press.

Ishii, M., Shearer, P. M., Houston, H., & Vidale, J. E. (2005). Extent, duration and speed of the 2004 Sumatra–Andaman earthquake imaged by the Hi-Net array. *Nature*, *435*, 933–936.

Jhingran, A. G. (1953). A note on the earthquake in the Andaman Islands (26 June 1941). *Records of the Geological Survey of India*, *82*, 300–307.

Kagan, Y. Y. (1991). 3-D rotation of double-couple earthquake sources. *Geophysical Journal International*, *106*, 709–716.

Kanamori, H. (1977). The energy release in great earthquakes. *Journal of Geophysical Research*, *82*, 2981–2987.

Lorito, S., Piatanesi, A., Cannelli, V., Romano, F., & Melini, D. (2010). Kinematics and source zone properties of the 2004 Sumatra-Andaman earthquake and tsunami: Nonlinear joint inversion of tide gauge, satellite altimetry, and GPS data. *Journal of Geophysical Research*, *115*(B2), B02304.

Mansinha, L., & Smylie, D. E. (1971). The displacement fields of inclined faults. *Bulletin of the Seismological Society of America*, *61*, 1433–1440.

Murty, T.S. (1984). Storm surges: Meteorological ocean tides, Can. Bull. Fisheries Aquat. Sci., 212, Dept. Fisheries Oceans, Ottawa.

Murty, T. S., & Rafiq, M. (1991). A tentative list of tsunamis in the Indian Ocean. *Natural Hazards*, *4*, 81–83.

Okal, E. A. (2005). A re-evaluation of the great Aleutian and Chilean earthquakes of 1906 August 17. *Geophysical Journal International*, *161*, 268–282.

Okal, E. A. (2015). Historical seismograms: Preserving an endangered species. *GeoResJ*, *6*, 53–64.

Okal, E. A., Kirby, S. H., & Kalligeris, N. (2016). The Showa Sanriku earthquake of 1933 March 2: A global seismological reassessment. *Geophysical Journal International*, *206*, 1492–1514.

Okal, E. A., & Saloor, N. (2017). Historical tsunami earthquakes in the Southwest Pacific: An extension to $\Delta > 80°$ of the Energy-to-Moment parameter Θ. *Geophysical Journal International*, *210*, 852–873.

Okal, E. A., & Stein, S. (2009). Observations of ultra-long period normal modes from the 2004 Sumatra-Andaman earthquake. *Physics of the Earth and Planetary Interiors*, *175*, 53–62.

Okal, E. A., & Synolakis, C. E. (2008). Far-field tsunami hazard from mega-thrust earthquakes in the Indian Ocean. *Geophysical Journal International*, *172*, 995–1015.

Okal, E. A., & Talandier, J. (1989). M_m: A variable period mantle magnitude. *Journal of Geophysical Research*, *94*, 4169–4193.

Ortíz, M., & Bilham, R. (2003). Source area and rupture parameters of the 31 December 1881 $M_w = 7.9$ Car Nicobar earthquake estimated from tsunamis recorded in the Bay of Bengal. *Journal of Geophysical Research*, *108*(B4), 2215.

Rajendran, C. P. (2013). Was the 1941 Andaman earthquake tsunamigenic? Comments on "Inundation studies for Nagapattinam region on the East coast of India due to tsunamigenic earthquakes from the Andaman region" by Srivastava et al. *Natural Hazards*, *65*, 981–984.

Ramana Murthy, M. V., Usha, T., Pari, Y., & Reddy, N. T. (2011). Tsunami vulnerability assessment of Cuddalore using numerical model and GIS. *Marine Geodesy*, *34*, 16–28.

Rees, B. A., & Okal, E. A. (1987). The depth of the deepest historical earthquakes. *Pure and Applied Geophysics*, *125*, 699–715.

Reymond, D., & Okal, E. A. (2000). Preliminary determination of focal mechanisms from the inversion of spectral amplitudes of mantle waves. *Physics of the Earth and Planetary Interiors*, *121*, 249–271.

Richter, C. F. (1958). *Elementary seismology*. San Francisco: Freeman.

Ritsema, A. R., & Veldkamp, J. (1960). Fault plane mechanisms of Southeast Asian earthquakes. *Publ. Koninkl. Nederl. Meteorolog. Inst.*, *72*, 63. (De Bilt).

Saito, T., & Furumura, T. (2009). Three-dimensional tsunami generation simulation due to sea-bottom deformation and its interpretation based on the linear theory. *Geophysical Journal International*, *178*, 877–888.

Salaree, A., & Okal, E. A. (2018). The "tsunami earthquake" of 13 April 1923 in Northern Kamchatka: Seismological and hydrodynamic investigations. *Pure and Applied Geophysics*, *175*, 1257–1285.

Sella, G. F., Dixon, T. H., & Mao, A. (2002). REVEL: A model for Recent plate velocities from space geodesy. *Journal of Geophysical Research*, *107*(B4), ETG-11.

Smyshlyaev, A. A. (2003). *Vremya krasnoĭ ryby*, pp. 310–315. Petropavlovsk-Kamchatskiĭ: Novaya Kniga [in Russian].

Srivastava, K., Krishna Kumar, R., Swapna, M., Swaroopa Rani, V., & Dimri, V. P. (2012). Inundation studies for Nagapattinam region on the East coast of India due to tsunamigenic earthquakes from the Andaman region. *Natural Hazards*, *63*, 211–221.

Storchak, D. A., Di Giacomo, D., Engdahl, E. R., Harris, J., Bondár, I., Lee, W. H. K., et al. (2015). The ISC-GEM global instrumental earthquake catalogue (1900–2009): Introduction. *Physics of the Earth and Planetary Interiors*, *239*, 48–63.

Synolakis, C. E. (2003). Tsunami and seiche. In W.-F. Chen & C. Scawthron (Eds.), *Earthquake engineering handbook* (pp. 9_1–9_90). Boca Raton: CRC Press.

Synolakis, C., Bernard, E., Titov, V., Kânoğlu, U., & González, F. (2008). Validation and verification of tsunami numerical models. *Pure and Applied Geophysics*, *165*, 2197–2228.

Titov, V., Kânoğlu, U., & Synolakis, C. (2016). Development of MOST for real-time tsunami forecasting. *Journal of Waterway Port Coastal and Ocean Engineering*, *142*(6), 03116004.

Titov, V. V., & Synolakis, C. E. (1998). Numerical modeling of tidal wave runup. *Journal of Waterway Port Coastal and Ocean Engineering*, *124*, 157–171.

Tsai, V. C., Nettles, M., Ekström, G., & Dziewonski, A. M. (2005). Multiple CMT source analysis of the 2004 Sumatra earthquake. *Geophysical Research Letters*, *32*(17), L17304.

Wessel, P., & Smith, W. H. F. (1991). Free software helps map and display data. *Eos Transactions American Geophysical Union*, *72*, 441 and 445–446.

Wickens, A.J., & Hodgson, J.H. (1967). *Computer re-evaluation of earthquake mechanism solutions, 1922–1962*. Publications of the Dominion Observatory, Ottawa (vol. 33, no. 1). Ottawa: Dept. Energy, Mines, Res.

Wysession, M. E., Okal, E. A., & Miller, K. L. (1991). Intraplate seismicity of the Pacific Basin, 1913–1988. *Pure and Applied Geophysics*, *135*, 261–359.

(Received October 16, 2018, revised December 18, 2018, accepted December 19, 2018, Published online January 17, 2019)